

Nonlinearity-Induced Reciprocity Breaking in a Single Nonmagnetic Taiji Resonator

A. Muñoz de las Heras^{1,*}, R. Franchi¹, S. Biasi², M. Ghulinyan¹, L. Pavesi², and I. Carusotto¹

¹*INO-CNR BEC Center and Dipartimento di Fisica, Università di Trento, 38123 Trento, Italy*

²*Nanoscience Laboratory, Dipartimento di Fisica, Università di Trento, 38123 Trento, Italy*

³*Centre for Materials and Microsystems, Fondazione Bruno Kessler, 38123 Trento, Italy*

(Received 19 January 2021; revised 19 April 2021; accepted 3 May 2021; published 19 May 2021)

We report on the demonstration of an effective, nonlinearity-induced nonreciprocal behavior in a single nonmagnetic multi-mode Taiji resonator. Nonreciprocity is achieved by a combination of an intensity-dependent refractive index and of a broken spatial reflection symmetry. Continuous wave power-dependent transmission experiments show nonreciprocity and a direction-dependent optical bistability loop. These can be explained in terms of the unidirectional mode coupling that causes an asymmetric power enhancement in the resonator. The observations are quantitatively reproduced by a numerical finite-element theory and physically explained by an analytical coupled-mode theory. This nonlinear Taiji resonator has the potential of being the building block of large arrays for the study of topological and/or non-Hermitian physics. This represents an important step towards the miniaturization of nonreciprocal elements for photonic integrated networks.

DOI: 10.1103/PhysRevApplied.15.054044

I. INTRODUCTION

Lorentz reciprocity is a fundamental property of electromagnetic fields propagating in linear and nonmagnetic media [1]. In optics, it imposes that transmission through any device built by such media is independent of the direction of propagation. However, nonreciprocal elements such as optical isolators and circulators [2,3] play a crucial role in a variety of technological applications, from unidirectional lasers to high-speed optical communications and information processing systems [4–6]. The usual path to optical nonreciprocity relies on employing magnetic elements that explicitly break the time-reversal \mathcal{T} symmetry [7–13]. Owing to the technical challenges associated with the monolithic integration of such elements into integrated photonics devices, alternative strategies compatible with state-of-the-art photonic technologies are being explored to circumvent Lorentz reciprocity. Time-dependent modulations of the material refractive index have been used but their operation requires an external driving field for the modulation and a large on-chip footprint [14–18]. As the reciprocity theorem crucially relies on the linearity of the field equations, another promising avenue is to exploit optical nonlinearities of materials. A first configuration involved a cascade of two nonlinear resonators with different properties, which made transmission strongly direction-dependent [19]. Similar nonreciprocal devices

were then studied exploiting complex resonator designs [20,21], \mathcal{PT} -symmetric coupled cavities [22,23], and two-beam interactions [24,25]. Related nonlinearity-induced topology and unidirectional propagation phenomena were experimentally realized in [26].

In this paper, we combine material nonlinearities and a broken spatial reflection symmetry to observe an effective breaking of Lorentz reciprocity in a single multi-mode Taiji resonator. Taiji micro-ring resonators (TJRs) are formed by a micro-ring with an S-shaped waveguide across as sketched in Fig. 1(a). In the presence of (saturable) gain, TJRs have been widely exploited to obtain unidirectional operation in ring laser devices [27–29] and, very recently, as the basic building block of complex lattice structures acting as topological lasers [30]. In the linear regime, reciprocity of the transmission across a TJR coupled to a bus waveguide is preserved and the effect of the S-shaped waveguide element is limited to an efficient unidirectional reflection [31]. Still, different optical powers are accumulated in the TJR depending on the direction of illumination [Figs. 1(b) and 1(c)]. At large input powers this leads to a direction-dependent effective nonlinearity and, thus, to an effective nonreciprocal transmission. In addition to providing an intuitive explanation to the mechanism underlying this key nonreciprocal behavior, we also show the important practical advantages offered by TJR-based nonreciprocal elements in silicon photonics: a smaller footprint than previous nonmagnetic proposals; an intrinsic degeneracy of the resonator modes which is

* a.munozdelasheras@unitn.it

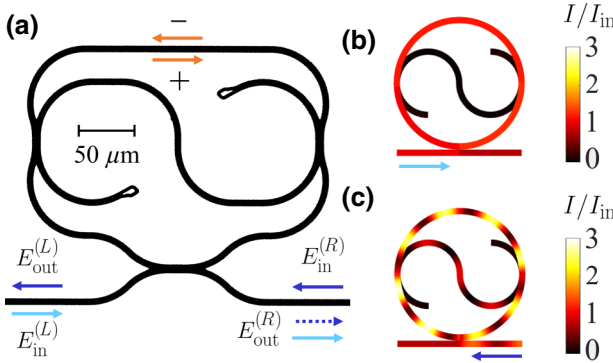


FIG. 1. (a) Optical image of the Taiji resonator (TJR) coupled to a bus waveguide. In the *forward* configuration (light blue arrows) light enters the sample from the left; in the *reverse* configuration (dark blue arrows) light is injected from the right. The dashed arrow represents the reflected light in the reverse case. The orange arrows indicate the propagation direction of clockwise (+) and counterclockwise (-) modes. (b),(c) Simulated intensity I (in units of the input intensity I_{in}) inside a TJR operating in the forward (b) and reverse (c) configurations for the same excitation frequency and power. The intensity maps are produced using the finite-element approach of Eq. (3).

protected by \mathcal{T} -reversal without the need for any fine tuning of the resonant frequencies of several devices; a reduced power threshold to nonreciprocity due to the use of the inter-mode nonlinearity and of the spatial overlap of the two degenerate modes.

The structure of the article is as follows. In Sec. II we develop an analytical coupled-mode theory of light propagation across the TJR and we make use of it to illustrate the reciprocity breaking for a TJR operating in the nonlinear regime. Section III presents all technical details of the experimental samples and the optical setup and summarizes the finite-element model used to describe *ab initio* the light propagation in our device. The experimental results are shown in Sec. IV and compared with the theory. Conclusions are finally drawn in Sec. V.

II. THEORY

As shown in Fig. 1(a), a TJR supports whispering-gallery modes propagating in clockwise (CW) and counterclockwise (CCW) directions, whose pairwise degeneracy is protected by \mathcal{T} -reversal. The effect of the S-shaped waveguide is to unidirectionally couple light from the CW mode into the CCW mode, whereas both modes display the same effective loss rate. In the *forward* configuration, light accesses the bus waveguide from its left side and excites the CCW mode of the resonator through a directional coupler, but does not propagate into the S-shaped waveguide. On the other hand, in the *reverse* configuration light enters the bus waveguide from the right and excites the CW mode; via the S-shaped waveguide it partially transfers

excitation into the CCW mode. The resulting increase of the total light intensity stored in the resonator is at the heart of the Lorentz reciprocity breaking.

A simplified model can guide our experimental analysis. Focusing on the neighborhood of a TJR resonance (resonance frequency ω_0), let us assume a monochromatic excitation at ω , a weak coupling of the micro-ring to the S-shaped waveguide and to the bus waveguide (real-valued coupling coefficients $k_S, k_w \ll 1$), and a power-dependent refractive index of the TJR $n = n_L + n_{\text{NL}}I$, where I is the optical intensity in the TJR [Figs. 1(b) and 1(c)] and n_L and n_{NL} are the linear refractive index and the nonlinear coefficient. We can adopt the widely used temporal coupled-mode theory [32,33] and write the steady-state electric field amplitudes E_{\pm} in the CW (+) and CCW (-) modes as

$$\begin{aligned} \omega E_+ &= \omega_0 E_+ - \frac{n_{\text{NL}}}{n_L} \omega_0 (|E_+|^2 + g|E_-|^2) E_+ - i\gamma_T E_+ \\ &\quad - \frac{c}{Ln_L} k_w E_{\text{in}}^{(R)}, \end{aligned} \quad (1)$$

$$\begin{aligned} \omega E_- &= \omega_0 E_- - \frac{n_{\text{NL}}}{n_L} \omega_0 (|E_-|^2 + g|E_+|^2) E_- - i\gamma_T E_- \\ &\quad - \frac{c}{Ln_L} k_w E_{\text{in}}^{(L)} - i \frac{c}{Ln_L} 2k_S^2 e^{i(\omega/c)n_L L_S} E_+. \end{aligned} \quad (2)$$

Here, L and L_S are the micro-ring and the S-shaped waveguide lengths, c is the vacuum speed of light, γ_T is the TJR loss rate (see later), $E_{\text{in}}^{(L)}$ and $E_{\text{in}}^{(R)}$ are the input fields exciting the ring from the left and the right of the bus waveguide, whereas the output fields to the left and to the right are $E_{\text{out}}^{(L)} = \sqrt{1 - k_w^2} E_{\text{in}}^{(R)} + ik_w E_+$ and $E_{\text{out}}^{(R)} = \sqrt{1 - k_w^2} E_{\text{in}}^{(L)} + ik_w E_-$, respectively.

The strength of the nonlinearity is quantified by $n_{\text{NL}} = n_K + n_T$ which is the sum of the Kerr n_K and thermal n_T nonlinearities. Of particular interest is the parameter g which describes the nature of the TJR nonlinearity. Here $g = 2$ represents a spatially local Kerr nonlinearity [34–36], whereas $g = 1$ describes a thermo-optic nonlinearity [37]. Note that the thermo-optic nonlinearity is mediated by a homogeneous heating of the TJR depending on the total energy that is dissipated in it. As shown in Appendix A, intermediate situations in which both processes contribute to n_{NL} are described by $g = (2n_K + n_T)/(n_K + n_T)$. In our specific silicon-based TJR, we have $n_T \gg n_K$ and, thus, $g \simeq 1$.

The total effective loss rate $\gamma_T = \gamma_A + ck_w^2/(2Ln_L) + ck_S^2/(Ln_L)$ is the same for the CW and CCW modes. It results from the sum of absorption γ_A and radiative losses into the bus and the S-shaped waveguides. Yet, the last term of (2) shows the asymmetric mode coupling introduced by the S-shaped waveguide: although all light lost by the CCW mode into the S-shaped waveguide is radiated away, part of the light transferred by the CW mode

into the S-shaped waveguide is reinjected into the CCW mode. This is illustrated in Figs. 1(b) and 1(c): in the forward configuration, only the CCW mode is excited and no reflection occurs; in the reverse configuration, both modes are excited, and marked interference fringes are visible in the intensity profile. As a result, for the same frequency and input power, the unidirectional mode coupling leads to a larger intensity inside the TJR in the reverse configuration than in the forward one.

While this asymmetry does not affect reciprocity in the linear regime of weak excitations [31], it has a major impact on the nonlinear response to strong fields. In Fig. 2(a), we show the numerical prediction of the coupled-mode equations (1) and (2) for the internal power propagating in the ring $P_{\text{ring}} \simeq A\epsilon_0 c n_L (|E_+|^2 + |E_-|^2)/2$ (with A the waveguide cross section and ϵ_0 the vacuum permittivity). The input power $P \simeq A\epsilon_0 c n_L |E_{\text{in}}|^2/2$ is kept at constant values while the frequency is scanned downwards across a resonance in forward and reverse configurations. At low input power the usual Lorentzian peak is found, though, because of the S-shaped waveguide, the internal power P_{ring} is higher in the reverse configuration. For a larger input power, the nonlinear refractive index causes a shift of the resonance proportional to the TJR internal power. In our $n_{\text{NL}} > 0$ case, the shift is towards lower frequencies. At sufficiently large powers, both curves display a sudden downward jump right after the resonance, as typical in optical bistability [38–42]. Note that the position of the jump depends on the direction: the larger internal intensity in the reverse configuration allows for a larger shift of the resonance before jumping. This difference is responsible for a frequency window where the internal intensity in the two configurations is strikingly different.

This key feature is an example of the nonlinear breaking of reciprocity and is further illustrated in Fig. 2(b). Here, we show the simulated transmitted power P_T as a function of the input power P for a fixed incident frequency $\omega - \omega_0 \simeq -4\gamma_T$ in the optical bistability regime. As the input power grows, P_T displays a linear increase up to a threshold P_1 where a sudden jump down onto another stable solution occurs. On the way back, for decreasing P , the threshold P_2 for the upwards jump is such that $P_2 \ll P_1$. Thus, a bistability loop opens that can be understood as a metastability in a first-order phase transition. Once again, the different values of the internal intensity P_{ring} in the forward and reverse cases lead to markedly different values for P_1 and P_2 . This results in intensity windows where the transmitted powers in the two directions are very different, as shown in the inset.

III. SAMPLES AND OPTICAL SETUP

In order to verify our predictions, we fabricated integrated TJR devices using silicon oxynitride (SiON) single-mode channel waveguides as shown in Fig. 1(a) [31].

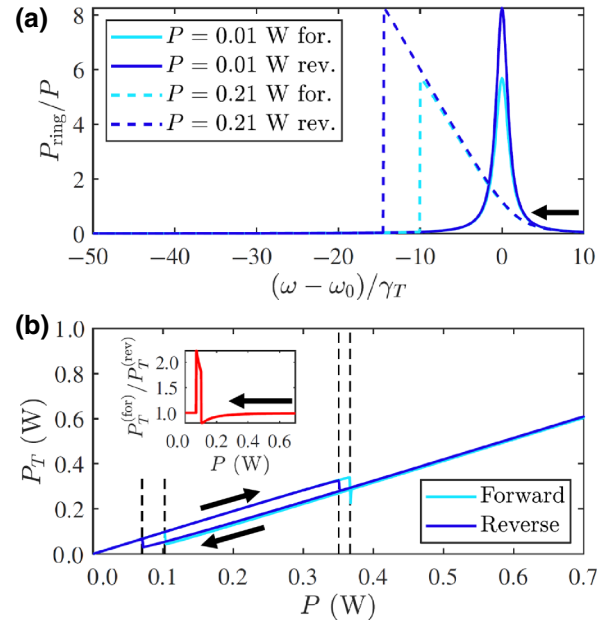


FIG. 2. (a) Simulated internal power P_{ring} for a downwards frequency sweep (black arrow) at two input powers P . Light (dark) blue curves refer to the forward (reverse) configuration. (b) Simulated transmitted power P_T for a fixed frequency $\omega - \omega_0 \simeq -4\gamma_T$ in the forward and reverse configurations. Black arrows indicate the sweep direction. Black dashed lines label the threshold powers. The inset shows the ratio $P_T^{(\text{for})}/P_T^{(\text{rev})}$ of the transmitted powers in the forward and reverse configurations along a decreasing P ramp. Parameters for both panels: $L \simeq 850 \mu\text{m}$, $L_S = L/2$, $k_w = k_S = 0.14$, $\gamma_A = 5.7 \times 10^9 \text{ s}^{-1}$, $n_L = 1.83$, $n_T = 8.8 \times 10^{-13} \text{ cm}^2/\text{W}$, $A = 0.66 \mu\text{m}^2$, and $g = 1$.

The waveguide cross section is $A = 0.66 \mu\text{m}^2$. As measured in [43] at a wavelength $\lambda \simeq 1550 \text{ nm}$, $n_L = 1.83$, and the linear absorption coefficient $\alpha = 0.35 \times 10^{-4} \mu\text{m}^{-1}$. We estimated $n_T = (8.8 \pm 0.4) \times 10^{-13} \text{ cm}^2/\text{W}$ from the fit of our experimental data, much larger than the typical Kerr nonlinear refractive index $n_K = 8 \times 10^{-16} \text{ cm}^2/\text{W}$ of the material [43]. The length of the bus waveguide is approximately the same on both sides of the TJR. In order to avoid undesired mode couplings, the ends of the S-shaped waveguide have been designed with a particular geometry [looking as rhomboids in Fig. 1(a)] which prevents back reflections [44].

The optical setup employs a fiber-coupled continuous wave tunable laser operating at the wavelength range spanning from 1490 to 1640 nm. Its output is coupled to an erbium-doped fiber amplifier to obtain high power. Then, a polarization control stage sets the input light to the transverse magnetic (TM) polarization. Light is coupled in the bus waveguide by butt coupling through a tapered fiber. The transmitted light is collected by a fiber and sent to an InGaAs detector. In order to switch between the forward and the reverse configurations, the sample is simply turned without any other change in the setup.

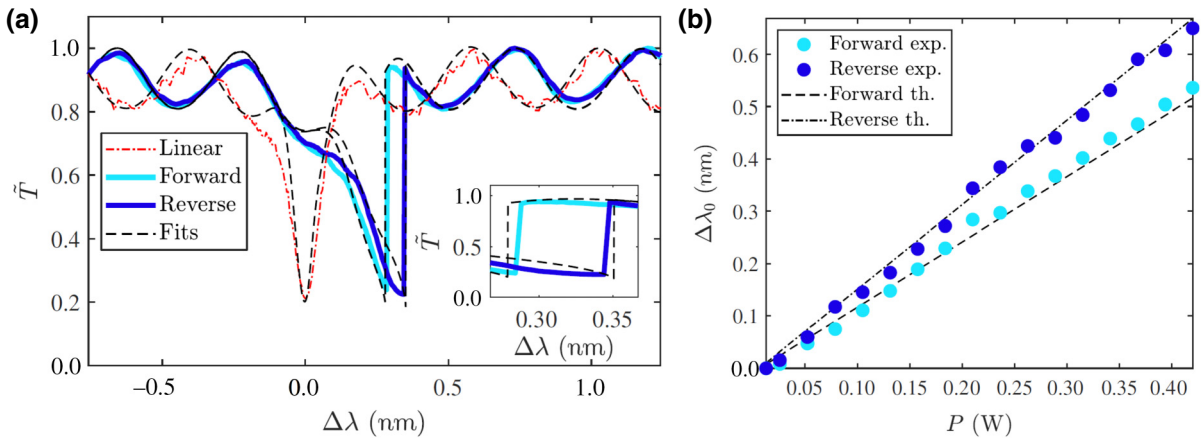


FIG. 3. (a) Normalized transmittance $\tilde{T} = T/T_{\max}$ as a function of the detuning $\Delta\lambda = \lambda - \lambda_0$ from the linear resonance wavelength for an upwards wavelength sweep (black arrow). The red dotted line represents the experimental transmittance in the linear regime for an input power $P \simeq 0.01$ W. The light (dark) blue solid curve corresponds to the experimental transmittance in forward (reverse) configuration at a fixed input power $P = 0.21$ W. The black dashed lines are theoretical fits of each experimental curve produced using Eq. (3). The inset gives a magnified view of the region of strongest nonreciprocal behavior. (b) Shift $\Delta\lambda_0$ of the resonance wavelength as a function of the input power P for the resonance displayed in panel (a). Light (dark) blue circles correspond to experimental data in forward (reverse) configuration. The black dashed (dotted) line is a linear fit to the theoretically calculated $\Delta\lambda_0$ in forward (reverse) configuration.

As reported in [31], the response of our samples is made more complicated by Fabry-Pérot oscillations in the transmittance due to reflections at the bus waveguide facets. Even though this does not affect the qualitative predictions of the coupled mode theory, a quantitative description requires taking this effect into account as well as relaxing other implicit approximations. To this purpose, we have built a more refined theory based on the solution of the nonlinear Helmholtz equation in our specific geometry. As detailed in Appendix B and in [31], the ring resonator as well as the S-shaped and the bus waveguides are appropriately segmented and propagation of the forward- and reverse-propagating waves along each segment of length $\Delta z \gg \lambda$ is described by the steady-state condition

$$E_{\pm}(z \pm \Delta z) = \exp \left\{ i \left[\left(n_L + i\alpha \frac{c}{\omega} \right) + n_T \frac{\Delta z}{L} \sum_{j=1}^N (|E_{\pm}(z_j)|^2 \right. \right. \\ \left. \left. + |E_{\mp}(z_j)|^2 \right] \frac{\omega}{c} \Delta z \right\} E_{\pm}(z), \quad (3)$$

where the thermo-optic nonlinear refractive index of each element results from the averaged power within it. Mixing of the field in the different elements is provided by directional couplers, whereas reflection at both ends of the bus waveguide is taken as lossless with reflection amplitude ik_m . As discussed in Appendix C, this finite-element theory matches the coupled-mode theory in the appropriate limits and can be used to quantitatively fit our experimental data.

IV. EXPERIMENTAL RESULTS

To probe the TJR response, we performed sweeps of the laser wavelength at fixed powers around the cold TJR resonance at $\lambda_0 = 1545.76$ nm. When operated at a small input power, $P \lesssim 0.03$ W, the thermal nonlinearity plays no role and the cold sample behaves as a linear device. Indeed, we observed the same transmittance T when pumped from the left or from the right. The linear transmittance normalized to its maximum value $\tilde{T} = T/T_{\max}$ is shown as a function of the detuning $\Delta\lambda = \lambda - \lambda_0$ from the resonance wavelength as the red dash-dotted line of Fig. 3(a). From a fit of this curve with the theoretical model (black dashed lines), we extracted the coefficients $k_w = 0.49 \pm 0.02$, $k_S = 0.14 \pm 0.03$, and $k_m = 0.24 \pm 0.04$. A list of all parameters employed in the fits of the experimental data can be found in Appendix D.

In order to investigate the nonlinear response, we then performed upwards wavelength ramps at larger input powers [an example for $P = 0.21$ W is shown in Fig. 3(a)]. As predicted by the model (Fig. 2), the resonance dip in \tilde{T} is pushed towards longer wavelengths by the nonlinearity due to the accumulated power in the TJR up to the threshold where \tilde{T} jumps back to a value close to one. In the reverse configuration, because a larger intensity is present inside the resonator for the same input power, the resonance wavelength experiences a larger displacement than in the forward configuration. This is our first evidence of a nonlinearity-induced nonreciprocal behavior. A magnified view around the transition points where the difference is the largest is shown in the inset of Fig. 3(a). Here, the ratio of the transmittance in the two directions reaches a

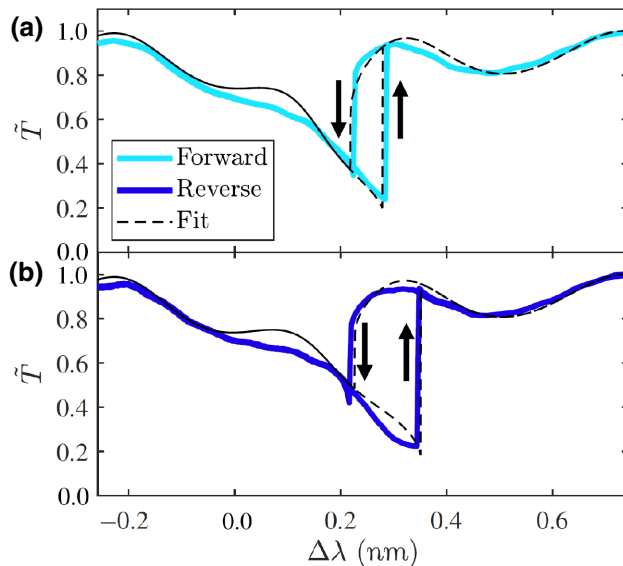


FIG. 4. Optical bistability in the normalized transmittance $\tilde{T} = T/T_{\max}$ along a round-trip sweep of the laser detuning $\Delta\lambda$ across the resonance at a fixed input power $P = 0.21$ W: (a) forward configuration (light blue); (b) reverse configuration (dark blue). The ramp direction is indicated by the black arrows. Experimental data are shown as solid lines whereas the black dashed lines are the fits obtained with the finite-element theory of Eq. (3).

value $T_{\text{for}}/T_{\text{rev}} \simeq 6$ dB at $\Delta\lambda \simeq 0.34$ nm. The displacement $\Delta\lambda_0$ of the resonance from its linear position as a function of the input power P is displayed in Fig. 3(b): the nonreciprocity is clearly visible as a larger slope in the reverse case because of the higher internal power. The small deviations of the experimental points (circles) from a linear fit of the theory (lines) are mostly due to the Fabry-Pérot oscillations. More details on the difference between the resonance shift shown in Fig. 3(b) and that produced by a Kerr nonlinearity of the same magnitude can be found in Appendix E.

Further insight in this physics is provided by the bistability loops that are observed when comparing the transmittance along frequency ramps in upwards and downwards directions at the same fixed input power. In agreement with the coupled-mode theory of Fig. 2, the experimental observations in Fig. 4 show that the bistable loop observed in the reverse configuration (bottom) is wider than that in the forward configuration (top), due to the different feedback caused by the S-shaped waveguide in the TJR. This is also reproduced by the finite-element model (dashed lines).

V. CONCLUSIONS

We have demonstrated how the combination of optical nonlinearities and a spatially asymmetric design gives rise to an effective violation of reciprocity in a single nonmagnetic multi-mode Taiji resonator. This device goes one step

beyond previous multi-resonator proposals and realizations in terms of integrability in silicon photonics circuits. The simplicity of its design allows a transparent theoretical analysis and facilitates its use as the unit cell of more complex structures.

The effective breaking of reciprocity is visible in the dependence of both the nonlinear shift of the resonance wavelength and the width of the optical bistability loop on the direction of illumination. The experimental observations are quantitatively reproduced by the theory and the effect is intuitively understood by a coupled-mode theory in terms of the asymmetric coupling introduced by the S-shaped waveguide and the consequently different strength of the nonlinear feedback effect.

Future work will address the technologically important issue of optimizing the nonreciprocity by employing Taiji resonators built of highly nonlinear materials in a properly designed critical coupling regime. The nonreciprocal bandwidth can also be extended by engineering an optimized coupling with the S-shaped waveguide allowing to achieve simultaneously a high-quality factor and a larger exchange of energy between the counterpropagating modes. Further prospective research lines will include building atop [45] to investigate the limitations set by dynamical reciprocity on the actual performance of our TJR device as a nonlinear optical isolator; and exploring the richer variety of nonlinearity-induced nonreciprocal effects in large arrays of resonators where they interplay with nontrivial band topologies and topological edge states [12,46]. On the long run, this will be ultimately extended to non-Hermitian systems with gains and losses [47].

ACKNOWLEDGMENTS

We acknowledge financial support from the Provincia Autonoma di Trento and the Q@TN initiative. S.B. acknowledges funding from the MIUR under the project PRIN PELM (20177 PSCKT). The authors would like to thank F. Ramiro Manzano, A. Calabrese and H. M. Price for continuous and insightful exchanges and E. Moser for technical support.

APPENDIX A: GENERAL COUPLED-MODE THEORY

The TJR coupled-mode theory steady-state equations in the most general case featuring a combination of local and nonlocal nonlinearities read

$$\begin{aligned} \omega E_+ &= \omega_0 E_+ - \frac{n_K}{n_L} \omega_0 (|E_+|^2 + 2|E_-|^2) E_+ \\ &\quad - \frac{n_T}{n_L} \omega_0 (|E_+|^2 + |E_-|^2) E_+ - i\gamma_T E_+ - \frac{c}{L n_L} k_w E_{\text{in}}^{(R)}, \end{aligned} \quad (\text{A1})$$

$$\begin{aligned} \omega E_- &= \omega_0 E_- - \frac{n_K}{n_L} \omega_0 (|E_-|^2 + 2|E_+|^2) E_- \\ &\quad - \frac{n_T}{n_L} \omega_0 (|E_-|^2 + |E_+|^2) E_- - i\gamma_T E_- - \frac{c}{L n_L} k_w E_{\text{in}}^{(L)} \\ &\quad - i \frac{c}{L n_L} 2k_S^2 e^{i(\omega/c)n_L L_S} E_+. \end{aligned} \quad (\text{A2})$$

By properly grouping both nonlinear terms it is easy to show that

$$\begin{aligned} \omega E_+ &= \omega_0 E_+ - \frac{n_K + n_T}{n_L} \omega_0 \left(|E_+|^2 + \frac{2n_K + n_T}{n_K + n_T} |E_-|^2 \right) \\ &\quad \times E_+ - i\gamma_T E_+ - \frac{c}{L n_L} k_w E_{\text{in}}^{(R)}, \end{aligned} \quad (\text{A3})$$

$$\begin{aligned} \omega E_- &= \omega_0 E_- - \frac{n_K + n_T}{n_L} \omega_0 \left(|E_-|^2 + \frac{2n_K + n_T}{n_K + n_T} |E_+|^2 \right) E_- \\ &\quad - i\gamma_T E_- - \frac{c}{L n_L} k_w E_{\text{in}}^{(L)} - i \frac{c}{L n_L} 2k_S^2 e^{i(\omega/c)n_L L_S} E_+, \end{aligned} \quad (\text{A4})$$

and, therefore,

$$n_{\text{NL}} = n_K + n_T, \quad g = \frac{2n_K + n_T}{n_K + n_T}. \quad (\text{A5})$$

Upon replacing $\omega \rightarrow i\partial_t$, these equations can be used to describe the evolution of the system in time under the assumption of a temporally local nonlinearity. Although this is usually a good approximation for Kerr media, one must keep in mind that thermal nonlinearities are typically slow so this approximation must be explicitly verified on a case-by-case basis.

APPENDIX B: FINITE-ELEMENT MODEL

In order to derive the finite-element equations to be employed in the fits of the experimental results we divided each waveguide in the sample into segments of equal length $\Delta z_{r,S,w} = L_{r,S,w}/N_{r,S,w} = z_j - z_{j-1}$, with $L_{r,S,w}$ (see [48]) being the total length of each component (ring, S , and bus waveguides), $N_{r,S,w}$ being the number of segments in which it is divided, and z_j being the spatial coordinate of each segment $j = 1, \dots, N_{r,S,w}$. The segment length in each case is assumed to be much longer than the light wavelength, i.e., $\Delta z_{r,S,w} \gg \lambda$. The aim of the finite-element model is to relate the amplitude of the electric field E at a position z_{j+1} to the amplitude in the precedent segment z_j . To simplify the notation, in the following we drop the subindices referring to the sample components as the equations are valid regardless of which waveguide is considered. We started from a modified Helmholtz's

equation including a local Kerr nonlinearity with refractive index n_K , and a nonlocal thermo-optical nonlinearity with refractive index n_T . It reads

$$\begin{aligned} \frac{\partial^2 E}{\partial z^2} &= - \left(\frac{\omega}{c} \right)^2 \left[\left(n_L + i\alpha \frac{c}{\omega} \right) + n_K |E(z)|^2 \right. \\ &\quad \left. + n_T \frac{\Delta z}{L} \sum_{j=1}^N |E(z_j)|^2 \right]^2 E(z), \end{aligned} \quad (\text{B1})$$

where ω and c correspond to the angular frequency and speed of light in free space, respectively, n_L is the linear refractive index, and α is the absorption coefficient. Note that the thermal nonlinearity shifts the refractive index at each sample component proportionally to the average intensity inside it. In our case, we have that $n_L \gg n_{K,T}|E(z)|^2 \forall z$, which implies that the field oscillation due to the linear part of the material's response will be much faster than that of the nonlinear part. Therefore, one can employ the Ansatz

$$\begin{aligned} E(z) &= E_+(z) + E_-(z) \\ &= \xi_+(z) e^{i(\omega/c)(n_L + i\alpha c/\omega)z} + \xi_-(z) e^{-i(\omega/c)(n_L + i\alpha c/\omega)z}, \end{aligned} \quad (\text{B2})$$

where E_{\pm} are the electric field amplitudes and ξ_{\pm} are the slowly evolving parts of the field propagating in the clockwise (+) and counterclockwise (-) directions.

After inserting Eq. (B2) into Eq. (B1) we use the rotating wave approximation to neglect those terms oscillating with spatial frequency on the order of ω/c or faster, which average to zero in a segment much longer than the optical wavelength, as well as the smaller terms proportional to $\partial^2 \xi_{+,-}/\partial z^2$ and those of order $\mathcal{O}(n_{K,T}^2)$. Identifying the energy-conserving processes we obtain

$$\begin{aligned} \frac{\partial \xi_{\pm}}{\partial z} &= \pm i \frac{\omega}{c} \left[n_K (|\xi_{\pm}(z)|^2 + 2|\xi_{\mp}(z)|^2) \right. \\ &\quad \left. + n_T \frac{\Delta z}{L} \sum_{j=1}^N (|\xi_{\pm}(z_j)|^2 + |\xi_{\mp}(z_j)|^2) \right] \xi_{\pm}(z). \end{aligned} \quad (\text{B3})$$

By integrating these differential equations along a single segment where the slowly evolving intensities $|\xi_{\pm}|^2$ can be considered as constant in our weak absorption regime and

employing the Ansatz (B2) one finally arrives to

$$E_{\pm}(z \pm \Delta z)$$

$$\begin{aligned} &= \exp \left\{ i \left[\left(n + i\alpha \frac{c}{\omega} \right) + n_K (|E_{\pm}(z)|^2 + 2|E_{\mp}(z)|^2) \right. \right. \\ &\quad \left. \left. + n_T \frac{\Delta z}{L} \sum_{j=1}^N (|E_{\pm}(z_j)|^2 + |E_{\mp}(z_j)|^2) \right] \frac{\omega}{c} \Delta z \right\} E_{\pm}(z). \end{aligned} \quad (\text{B4})$$

which generalizes Eq. (3) to generic nonlinearities. The fields in the different components of the sample are coupled in reciprocal and lossless directional couplers in which the output and input field amplitudes are related by a scattering matrix

$$\begin{pmatrix} E_{\text{out},1} \\ E_{\text{out},2} \end{pmatrix} = \begin{pmatrix} t_{w,S,m} & ik_{w,S,m} \\ ik_{w,S,m} & t_{w,S,m} \end{pmatrix} \begin{pmatrix} E_{\text{in},1} \\ E_{\text{in},2} \end{pmatrix}, \quad (\text{B5})$$

where $t_{w,S}$ and $ik_{w,S}$ represent the transmission and coupling amplitudes in the ring-bus and ring-S couplers, respectively. On the other hand, t_m and ik_m correspond to the transmission and reflection amplitudes at the facets of the bus waveguide, which give rise to Fabry-Pérot oscillations. Note that $t_{w,S,m}$ and $k_{w,S,m}$ are taken as real numbers satisfying $t_{w,S,m}^2 + k_{w,S,m}^2 = 1$.

Altogether, the set of Eqs. (B4) and (B5) for all elements of our setup represent the electric field propagation throughout the sample and can be solved with standard

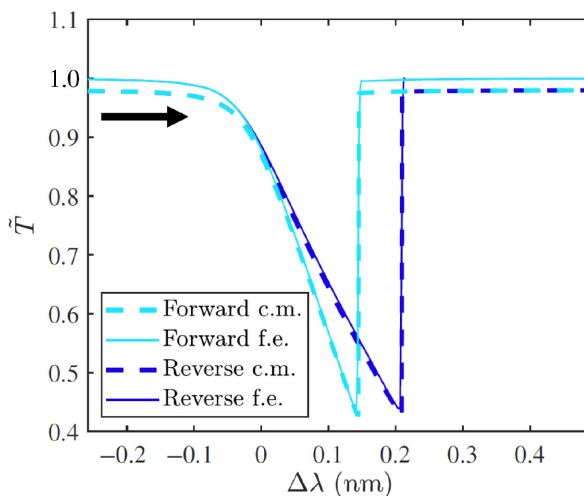


FIG. 5. Normalized transmittance \tilde{T} as a function of the relative wavelength shift with respect to the resonance wavelength ($\Delta\lambda$) in an upwards ramp (indicated by the black arrow) for a TJR in the forward (light blue) and reverse (dark blue) configurations. The dashed curves are calculated by using the coupled-mode theory (c.m.), whereas the solid lines are obtained with the finite-element model (f.e.). The incident power is taken to be $P = 0.21$ W. The parameters of the simulations are those of Fig. 2.

numerical techniques providing a complete and quantitative description of the nonlinear light propagation at the steady state.

APPENDIX C: COUPLED-MODE THEORY AND FINITE-ELEMENT MODEL IN THE WEAK COUPLING REGIME

In this appendix we show that the finite-element simulations recover the coupled-mode theory results in the weak coupling limit ($k_{w,S} \ll 1$) without Fabry-Pérot oscillations ($k_m = 0$). Figure 5 displays the normalized transmittance $\tilde{T} = T/T_{\max}$ for a TJR operating in forward and reverse configurations as obtained by using both formalisms. The parameters of the simulations are those employed in Fig. 2 for an incident power $P = 0.21$ W. The agreement between both models is best found around resonance where the coupled-mode equations are valid. The discontinuities and the nonreciprocal window are found to lie at the same wavelengths in both simulations.

APPENDIX D: FIT PARAMETERS

Table I summarizes the parameters employed in the fit of the experimental data using the finite-element model derived in Appendix B. A diagram of the simulated device is shown in Fig. 6. The TJR is assumed to be at the center of the bus waveguide. Although the sample employed in the experiment features an asymmetrical TJR with an optimized shape in order to reduce backscattering of light, to facilitate the calculations we employed a circular TJR with the same ring length.

TABLE I. Fit parameters: ring radius R_r , S waveguide radius R_S , bus waveguide length to the left L_L and right L_R of the TJR, waveguide cross section A , number of segments in which the ring, S, and bus waveguides are divided by $N_{r,S,w}$, linear refractive index n_L , nonlinear Kerr refractive coefficient n_K , nonlinear thermal refractive coefficient n_T , absorption losses α , coupling parameters $k_{w,S}$ for the ring-bus waveguide and ring-S waveguide couplers, and reflection amplitude k_m at the bus waveguide facets.

R_r	135.11 μm	n_L	1.83
R_S	62.45 μm	n_K	$8 \times 10^{-16} \text{ cm}^2/\text{W}$
L_L	687.50 μm	n_T	$(8.8 \pm 0.4) \times 10^{-13} \text{ cm}^2/\text{W cm}^2/\text{W}$
L_R	687.50 μm	α	$0.3454 \times 10^{-4} \mu\text{m}^{-1}$
A	$0.66 \times 10^{-8} \text{ cm}^2$	k_w	0.49 ± 0.02
N_r	8	k_S	0.14 ± 0.03
N_S	2	k_m	0.24 ± 0.04
N_w	4		

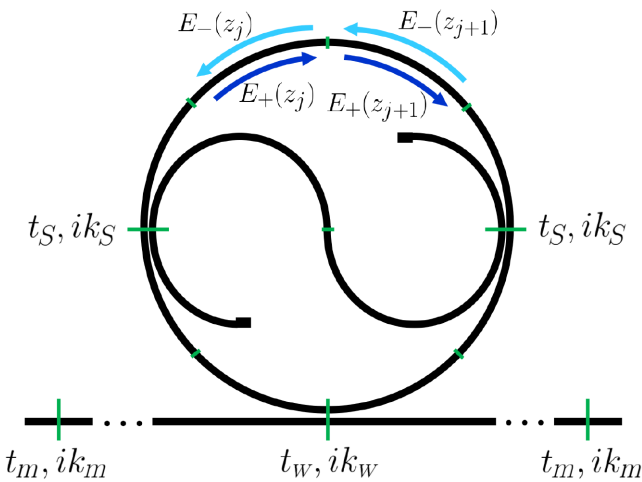


FIG. 6. Scheme of the modeled Taiji resonator (TJR) showing the electric field amplitudes E inside each segment z_j (delimited by the short transverse lines) and the transmission and coupling amplitudes at each directional coupler (represented by the long transverse lines) $t_{w,S,m}$ and $ik_{w,S,m}$.

APPENDIX E: RESONANCE SHIFT FOR EQUIVALENT THERMO-OPTIC AND KERR NONLINEARITIES

Here we compare the resonance shift $\Delta\lambda_0$ produced by the thermo-optic nonlinearity displayed by our samples with the one that would exhibit a (fictitious) TJR featuring a Kerr nonlinear parameter of the same magnitude $n_K = 8.8 \times 10^{-13} \text{ cm}^2/\text{W}$ and a negligible $n_T \simeq 0$. In all calculations, $\Delta\lambda_0$ is measured with respect to the linear position of the resonance at $\lambda = 1545.76 \text{ nm}$. Figure 7 shows linear fits of the numerical results of the finite-element model in each case, which slightly deviate from the linear behaviour due to Fabry-Pérot oscillations: quite unexpectedly, for a given value of the input power the Kerr nonlinearity with $g = 2$ gives a slightly smaller nonlinear shift $\Delta\lambda_0$ than the thermo-optic nonlinearity ($g = 1$).

These numerical results can be physically understood using the coupled-mode equations (1) and (2). In the forward configuration light circulates in the CCW mode only and no significant difference between both kinds of nonlinearity arises. In the reverse configuration, one could have expected that the presence of the $g = 2$ factor in the Kerr nonlinear term of Eq. (2) would give a larger nonlinear shift $\Delta\lambda_0$ compared with the thermo-optical case. The complete calculation displayed here shows that this is not the case, because the very presence of this factor $g = 2$ quickly pushes the CCW mode out of resonance from the CW one and the pump laser. This results in a smaller value of the intensity in the CCW mode, which may well overcompensate the factor of two. As a result, the net effective nonlinear shift $\Delta\lambda_0$ turns out to be a bit smaller for a Kerr nonlinearity than for a thermal one at the same input power.

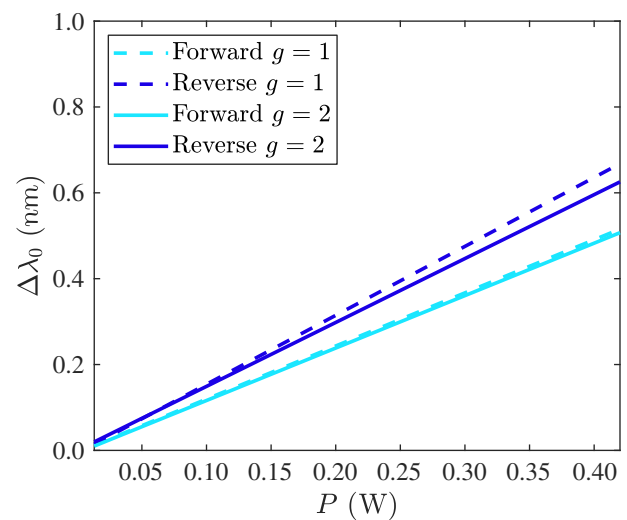


FIG. 7. Shift of the resonance wavelength $\Delta\lambda_0$ with respect to its linear value $\lambda = 1545.76 \text{ nm}$ as a function of the input power P . All curves are linear fits of the numerically calculated data using the finite-element model. Dashed lines are the curves displayed in Fig. 3(b) for the experimental case of a thermo-optic nonlinearity with $n_T = 8.8 \times 10^{-13} \text{ cm}^2/\text{W}$. Solid lines are obtained by employing a purely Kerr nonlinearity ($n_T = 0$) whose strength has been artificially increased to $n_K = 8.8 \times 10^{-13} \text{ cm}^2/\text{W}$ to match the strength of the thermo-optic nonlinearity of the experiment. Light (dark) blue lines correspond to the forward (reverse) configuration.

- [1] R. J. Potton, Reciprocity in optics, *Rep. Prog. Phys.* **67**, 717 (2004).
- [2] W. B. Ribbens, An optical circulator, *Appl. Opt.* **4**, 1037 (1965).
- [3] D. Jalas, A. Petrov, M. Eich, W. Freude, S. Fan, Z. Yu, R. Baets, M. Popović, A. Melloni, J. D. Joannopoulos, M. Vanwolleghem, C. R. Doerr, and H. Renner, What is—and what is not—an optical isolator, *Nat. Photonics* **7**, 579 (2013).
- [4] D. A. B. Miller, Rationale and challenges for optical interconnects to electronic chips, *Proc. IEEE* **88**, 728 (2000).
- [5] I. P. Kaminow, Optical integrated circuits: A personal perspective, *J. Lightwave Technol.* **26**, 994 (2008).
- [6] R. Nagarajan, M. Kato, J. Pleumeekers, P. Evans, S. Corzine, S. Hurtig, A. Dentai, S. Murthy, M. Missey, R. Muthiah, R. A. Salvatore, C. Joyner, R. Schneider, M. Ziari, F. Kish, and D. Welch, Inp photonic integrated circuits, *IEEE J. Sel. Top. Quantum Electron.* **16**, 1113 (2010).
- [7] H. Dötsch, N. Bahlmann, O. Zhuromskyy, M. Hammer, L. Wilkens, R. Gerhardt, P. Hertel, and A. F. Popkov, Applications of magneto-optical waveguides in integrated optics: Review, *J. Opt. Soc. Am. B* **22**, 240 (2005).
- [8] Z. Wang and S. Fan, Optical circulators in two-dimensional magneto-optical photonic crystals, *Opt. Lett.* **30**, 1989 (2005).

- [9] Z. Wang, Y. Chong, J. D. Joannopoulos, and M. Soljačić, Observation of unidirectional backscattering-immune topological electromagnetic states, *Nature* **461**, 772 (2009).
- [10] L. Bi, J. Hu, P. Jiang, D. H. Kim, G. F. Dionne, L. C. Kimerling, and C. A. Ross, On-chip optical isolation in monolithically integrated non-reciprocal optical resonators, *Nat. Photonics* **5**, 758 (2011).
- [11] Y. Shoji, M. Ito, Y. Shirato, and T. Mizumoto, MZI optical isolator with Si-wire waveguides by surface-activated direct bonding, *Opt. Express* **20**, 18440 (2012).
- [12] T. Ozawa, H. M. Price, A. Amo, N. Goldman, M. Hafezi, L. Lu, M. C. Rechtsman, D. Schuster, J. Simon, O. Zilberman, and I. Carusotto, Topological photonics, *Rev. Mod. Phys.* **91**, 015006 (2019).
- [13] W. Yan, Y. Yang, S. Liu, Y. Zhang, S. Xia, T. Kang, W. Yang, J. Qin, L. Deng, and L. Bi, Waveguide-integrated high-performance magneto-optical isolators and circulators on silicon nitride platforms, *Optica* **7**, 1555 (2020).
- [14] S. Bhandare, S. K. Ibrahim, D. Sandel, Hongbin Zhang, F. Wust, and R. Noe, Novel nonmagnetic 30-dB traveling-wave single-sideband optical isolator integrated in III/V material, *IEEE J. Sel. Top. Quantum Electron.* **11**, 417 (2005).
- [15] Z. Yu and S. Fan, Complete optical isolation created by indirect interband photonic transitions, *Nat. Photonics* **3**, 91 (2009).
- [16] K. Fang, Z. Yu, and S. Fan, Realizing effective magnetic field for photons by controlling the phase of dynamic modulation, *Nat. Photonics* **6**, 782 (2012).
- [17] C. Galland, R. Ding, N. C. Harris, T. Baehr-Jones, and M. Hochberg, Broadband on-chip optical non-reciprocity using phase modulators, *Opt. Express* **21**, 14500 (2013).
- [18] C. R. Doerr, L. Chen, and D. Vermeulen, Silicon photonics broadband modulation-based isolator, *Opt. Express* **22**, 4493 (2014).
- [19] L. Fan, J. Wang, L. T. Varghese, H. Shen, B. Niu, Y. Xuan, A. M. Weiner, and M. Qi, An all-silicon passive optical diode, *Science* **335**, 447 (2012).
- [20] A. Li and W. Bogaerts, Reconfigurable nonlinear nonreciprocal transmission in a silicon photonic integrated circuit, *Optica* **7**, 7 (2020).
- [21] P. Aleahmad, M. Khajavikhan, D. Christodoulides, and P. LiKamWa, Integrated multi-port circulators for unidirectional optical information transport, *Sci. Rep.* **7**, 2129 (2017).
- [22] B. Peng, Ş. K. Özdemir, F. Lei, F. Monifi, M. Giannfreda, G. L. Long, S. Fan, F. Nori, C. M. Bender, and L. Yang, Parity-time-symmetric whispering-gallery microcavities, *Nat. Phys.* **10**, 394 (2014).
- [23] L. Chang, X. Jiang, S. Hua, C. Yang, J. Wen, L. Jiang, G. Li, G. Wang, and M. Xiao, Parity-time symmetry and variable optical isolation in active-passive-coupled microresonators, *Nat. Photonics* **8**, 524 (2014).
- [24] L. Del Bino, J. M. Silver, S. L. Stebbings, and P. Del'Haye, Symmetry breaking of counter-propagating light in a nonlinear resonator, *Sci. Rep.* **7**, 43142 (2017).
- [25] L. D. Bino, J. M. Silver, M. T. M. Woodley, S. L. Stebbings, X. Zhao, and P. Del'Haye, Microresonator isolators and circulators based on the intrinsic nonreciprocity of the Kerr effect, *Optica* **5**, 279 (2018).
- [26] L. J. Maczewsky, M. Heinrich, M. Kremer, S. K. Ivanov, M. Ehrhardt, F. Martinez, Y. V. Kartashov, V. V. Konotop, L. Torner, D. Bauer, and A. Szameit, Nonlinearity-induced photonic topological insulator, *Science* **370**, 701 (2020).
- [27] J. P. Hohimer, G. A. Vawter, and D. C. Craft, Unidirectional operation in a semiconductor ring diode laser, *Appl. Phys. Lett.* **62**, 1185 (1993).
- [28] S. Kharitonov and C.-S. Brès, Isolator-free unidirectional thulium-doped fiber laser, *Light: Sci. Appl.* **4**, e340 (2015).
- [29] J. Ren, Y. G. N. Liu, M. Parto, W. E. Hayenga, M. P. Hokmabadi, D. N. Christodoulides, and M. Khajavikhan, Unidirectional light emission in PT-symmetric microring lasers, *Opt. Express* **26**, 27153 (2018).
- [30] M. A. Bandres, S. Wittek, G. Harari, M. Parto, J. Ren, M. Segev, D. N. Christodoulides, and M. Khajavikhan, Topological insulator laser: Experiments, *Science* **359**, 1231 (2018).
- [31] A. Calabrese, F. Ramiro-Manzano, H. M. Price, S. Biasi, M. Bernard, M. Ghulinyan, I. Carusotto, and L. Pavesi, Unidirectional reflection from an integrated “taiji” microresonator, *Photonics Res.* **8**, 1333 (2020).
- [32] D. Walls and G. Milburn, *Quantum Optics*, Springer Study Edition (Springer Berlin Heidelberg, New York, 2012).
- [33] M. Ghulinyan, F. R. Manzano, N. Prtljaga, M. Bernard, L. Pavesi, G. Pucker, and I. Carusotto, Intermode reactive coupling induced by waveguide-resonator interaction, *Phys. Rev. A* **90**, 053811 (2014).
- [34] R. Y. Chiao, P. L. Kelley, and E. Garmire, Stimulated Four-Photon Interaction and its Influence on Stimulated Rayleigh-Wing Scattering, *Phys. Rev. Lett.* **17**, 1158 (1966).
- [35] A. E. Kaplan, Light-induced nonreciprocity, field invariants, and nonlinear eigenpolarizations, *Opt. Lett.* **8**, 560 (1983).
- [36] G. N. Ghalanos, J. M. Silver, L. Del Bino, N. Moroney, S. Zhang, M. T. M. Woodley, A. O. Svela, and P. Del'Haye, Kerr-Nonlinearity-Induced Mode-Splitting in Optical Microresonators, *Phys. Rev. Lett.* **124**, 223901 (2020).
- [37] V. Ilchenko and M. L. Gorodetskii, Thermal nonlinear effects in optical whispering gallery microresonators, *Laser Phys.* **2**, 1004 (1992).
- [38] R. W. Boyd, *Nonlinear Optics* (Academic Press, Cambridge, Massachusetts, 2008).
- [39] P. N. Butcher and D. Cotter, *The Elements of Nonlinear Optics*, Cambridge Studies in Modern Optics (Cambridge University Press, Cambridge, England, 2008).
- [40] H. M. Gibbs, *Optical Bistability: Controlling Light with Light* (Academic Press, Cambridge, Massachusetts, 1985).
- [41] F. Ramiro-Manzano, N. Prtljaga, L. Pavesi, G. Pucker, and M. Ghulinyan, Thermo-optical bistability with Si nanocrystals in a whispering gallery mode resonator, *Opt. Lett.* **38**, 3562 (2013).
- [42] M. Bernard, F. R. Manzano, L. Pavesi, G. Pucker, I. Carusotto, and M. Ghulinyan, Complete crossing of Fano resonances in an optical microcavity via nonlinear tuning, *Photonics Res.* **5**, 168 (2017).

- [43] A. Trenti, M. Borghi, S. Biasi, M. Ghulinyan, F. Ramiro-Manzano, G. Pucker, and L. Pavesi, Thermo-optic coefficient and nonlinear refractive index of silicon oxynitride waveguides, [AIP Adv. 8, 025311 \(2018\)](#).
- [44] C. Castellan, S. Tondini, M. Mancinelli, C. Kopp, and L. Pavesi, Reflectance reduction in a whiskered SOI star coupler, [IEEE Photonics Technol. Lett. 28, 1870 \(2016\)](#).
- [45] Y. Shi, Z. Yu, and S. Fan, Limitations of nonlinear optical isolators due to dynamic reciprocity, [Nat. Photonics 9, 388 \(2015\)](#).
- [46] D. Smirnova, D. Leykam, Y. Chong, and Y. Kivshar, Nonlinear topological photonics, [Appl. Phys. Rev. 7, 021306 \(2020\)](#).
- [47] M. Parto, Y. G. N. Liu, B. Bahari, M. Khajavikhan, and D. N. Christodoulides, Non-hermitian and topological photonics: Optics at an exceptional point, [Nanophotonics 10, 403 \(2021\)](#).
- [48] Note that here and in the following we use the compact notation of repeated indices for different quantities, i.e., $L_{r,S,w}$ corresponds to L_r , L_S and L_w .